

Hybrid-order topology with tunable chiral hinge modes and unpinned Dirac surface states in the altermagnetic insulator $\text{Eu}_3\text{In}_2\text{As}_4$

Yufei Zhao,¹ Hyeonhu Bae,¹ Yiyang Jiang,¹ Yongkang Li,¹ Chao-Xing Liu,² and Binghai Yan^{1,*}

¹*Department of Condensed Matter Physics, Weizmann Institute of Science, Rehovot 7610001, Israel*

²*Department of Physics, the Pennsylvania State University, University Park, PA 16802, USA*

The exploration of magnetic topological states is instrumental in exploring axion electrodynamics and intriguing transport phenomena, such as the quantum anomalous Hall effect. Here, we predict that the recently-synthesized material $\text{Eu}_3\text{In}_2\text{As}_4$ exhibits as both an axion insulator and a 3D Stiefel-Whitney insulator with an altermagnetic order. When spins align in the ab plane, we find an unpinned surface Dirac cone on the ab plane and chiral hinge states along the c direction, where hinge states can generate a half-quantized surface anomalous Hall effect on the ac and bc facets. When spins align along c , we observe a mirror-protected topological crystalline insulator. Furthermore, the ferromagnetic phase, in which spins are aligned in the same direction by an external in-plane magnetic field, presents an ideal Weyl semimetal with a single pair of type-I Weyl points and no extra Fermi pocket. Our work predicts rich topological states tuned by magnetic structures in $\text{Eu}_3\text{In}_2\text{As}_4$, supporting the further study of the topological transport and Majorana fermions in proximity to a superconductor.

I. INTRODUCTION

Topological quantum states of matter are usually characterized by unique boundary states following the bulk-boundary correspondence [1–3]. For example, a topological insulator (TI) exhibits 2D Dirac-type surface states [4, 5] and a higher-order TI (HOTI) shows 1D hinge states [6–8]. Here, we report a magnetic TI material that hosts both topological surface states and chiral hinge states, dubbed a hybrid-order magnetic TI, which is protected by the combined symmetry between rotational and time-reversal symmetry [9–12].

Unlike nonmagnetic HOTIs [6, 7, 13–16], hinge modes in a magnetic topological crystalline insulator (TCI) are intimately related to magnetic structures, by which the direction or chirality of currents can be manipulated [8]. For instance, applying a magnetic field to flip or rotate spin moments is equivalent to reversing the mass signs of the gapped surface, and thus switching the chirality of hinge states and the mapped 2D Chern number [17–19]. Identifying the nature of topological invariants under a combined magnetic crystalline symmetry by the translation (τ) or n -fold rotation (C_n) with time-reversal (\mathcal{T}), is evidently a central issue, exemplified by $\tau\mathcal{T}$ protected \mathbb{Z}_2 antiferromagnetic (AFM) TI [20–23]. Recent theory shows that a $C_2\mathcal{T}$ protected TCI holds both the robust gapless surface states and chiral hinge states [9–12] while its material realization is still missing.

Furthermore, a magnetic TCI can generate axion electrodynamics, described by the so-called θ term [24, 25]

$$S_\theta = \int dt d^3x \frac{\theta e^2}{4\pi^2 \hbar c} \mathbf{E} \cdot \mathbf{B}, \quad (1)$$

where \mathbf{E} and \mathbf{B} are external electric and magnetic fields, θ is the axion field defined in a 3D system. When \mathcal{T} is broken, but inversion (\mathcal{I}) or a combined symmetry (e.g. $\tau\mathcal{T}$, $C_n\mathcal{T}$, $C_n\mathcal{I}$) is preserved, the axion field is odd so that θ is quantized to be 0 or π , which corresponds to trivial insulators and axion insulators [20, 21, 26–29]. With gapped surface states, axion insulators manifest half-quantized surface anomalous Hall conductance (AHC) of $\pm e^2/2h$. When two adjacent gapped surfaces hold opposite signs of mass, the Hall effect is carried by the 1D chiral mode at the hinge [3, 7, 24, 30–33].

Despite the intriguing interplay of topology and magnetism, the material realization of axion insulators is still challenging. External magnetic doping, proximity, and a few classes of stoichiometric intrinsic magnetic candidates have been proposed in the past few years [3, 34–42]. In EuIn_2As_2 and $\text{EuSn}_2(\text{As,P})_2$, the experimental signatures of band inversion, AFM order, and spin spiral states have been reported [18, 43–47]. Unlike MnBi_2Te_4 , Eu-based Zintl compounds belong to another axion insulator family. As discussed later, their altermagnetic order, where the opposite-spin sublattices are connected by rotation symmetry instead of \mathcal{IT} or $\tau\mathcal{T}$ [48–51], require us to further understand the symmetry-related topology.

In this work, we predict that $\text{Eu}_3\text{In}_2\text{As}_4$, an altermagnet in the ground state, is a hybrid-order TCI with tunable chiral hinge states and unpinned Dirac surface states, classified as a $C_2\mathcal{T}$ -protected Stiefel-Whitney (SW) insulator [10, 11]. Rotating the magnetic moments in the ab plane can manipulate the Dirac cone position on the ab plane. Chiral hinge states appear along the c direction and lead to half-quantized surface anomalous Hall effect in the ac and bc facets, manifesting the axion insulator state. Rotating the magnetic field from in-plane to out-of-plane gaps the Dirac point. We further reveal an ideal Weyl semimetal phase in the ferromagnetic (FM) phase and identify the universal topological feature in the Eu-based Zintl

* Corresponding author: binghai.yan@weizmann.ac.il

family of topological materials. Additionally, $\text{Eu}_3\text{In}_2\text{As}_4$ was recently grown from InAs nanowires in a mutual-exchange method [52] and inherits the ideal proximity with a superconductor [53]. Thus, this material will provide a platform to study possible Majorana modes due to the interplay between chiral hinge states/Dirac surface states and superconductivity.

II. CRYSTAL, MAGNETIC, AND BULK BAND STRUCTURES

The Zintl compound $\text{Eu}_3\text{In}_2\text{As}_4$ has an orthorhombic lattice and the corresponding space group ($Pnmm$, No. 58) includes inversion \mathcal{I} , a twofold rotation C_{2z} and a mirror symmetry M_z , and nonsymmorphic symmetries $\{C_{2x,2y}|\tau\}$, $\{M_{x,y}|\tau\}$, where τ is the translation of one-half of a body diagonal $(\frac{a}{2}, \frac{b}{2}, \frac{c}{2})$. As shown in Fig. 1(a), all atoms are located at $z = 0$ and $z = 0.5$ planes, and one In atom and four nearest neighboring (NN) As atoms form a tetrahedron. The tetrahedrons ($[\text{In}_2\text{As}_4]^{6-}$) constitute a 1D chain by sharing their corners along the c axis, between which the divalent Eu^{2+} cations are dispersed. Three Eu atoms (a trimer linked by the dashed line) with two NN tetrahedrons tend to form a sublattice. Within one unit cell, two sublattices are related by $\{C_{2x,2y}|\tau\}$ or $\{M_{x,y}|\tau\}$ operations. In density-functional theory (DFT) calculations, lattice parameters are optimized within 1% error compared to experimental values [54]. The energy bands near the Fermi level are mainly from In-5s and As-4p orbitals.

We first examine the magnetic ground state of $\text{Eu}_3\text{In}_2\text{As}_4$. Eu^{2+} shows $\mathbf{S} = 7 \mu_B$ magnetic moment. Localized Eu-4f orbitals appear between -2.5 eV and -1.5 eV below the Fermi energy for DFT+ U calculations tested with different U values [Supplemental Material (SM) Fig. S2]. We found that the AFM phase is the magnetic ground state while the FM phase is energetically less favorable (see Fig. 1(b)). In the AFM phase, Eu^{2+} cations exhibit FM coupling along the c -axis but a staggered AFM order inside the trimer. Two sublattices are linked via $\{C_{2y}|\tau\}$ and also AFM coupled. Thus, $\text{Eu}_3\text{In}_2\text{As}_4$ is an altermagnet [48–51], and allows the lifted spin degeneracy along some k -path. A small magnetic anisotropy exists for magnetic moments along a, b, c directions. When the easy axis is along a/b axis (AFM a/b state), a time-reversal \mathcal{T} requires to combine with C_{2z} , M_z , $\{C_{2x/y}|\tau\}$ and $\{M_{x/y}|\tau\}$. Complete symmetry operations can be found in Supplementary Table II for different magnetic structures. The AFM order is consistent with a recent experiment [52].

We next investigate the band structure and topology under the altermagnetic order (dubbed “AFM” hereafter). In Fig. 1(c), without spin-orbit coupling (SOC), a trivial bandgap of 52 meV is found at Γ point, and spin-split bands caused by the altermagnetic order are found along $\Gamma - S$ direction (see SM Fig. S3). In the AFM c phase, the presence of SOC induces an inverted gap of

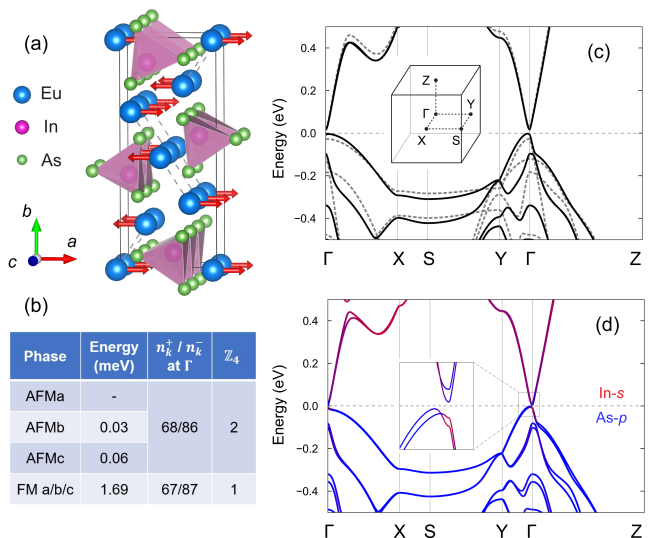


FIG. 1. (a) Crystal structure of $\text{Eu}_3\text{In}_2\text{As}_4$ in the AFM a phase. As an altermagnet, spin sublattices are related by the $\{C_{2y}|\tau\}$ symmetry rather than inversion or translation. The a, b, c crystallographic axes point to x, y, z directions. (b) The relative energy difference per Eu for different magnetic phases and corresponding \mathbb{Z}_4 topological invariant from the parity eigenvalues, showing an axion insulator in the AFM phase and a Weyl semimetal in the FM phase. (c) The band structure of $\text{Eu}_3\text{In}_2\text{As}_4$ without (grey dashed) and with (black solid) SOC for the AFM c phase. The inset is the bulk Brillouin zone (BZ). (d) The band structure for the AFM a phase with the projection of In- s and As- p orbitals.

21 meV at Γ . The two-fold degenerate bands are found at $k_z = 0$ plane and along $\Gamma - Z$, since $\{M_{x,y}|\tau\}$ anti-commutes with M_z , and $\{C_{2x,2y}|\tau\}$ anti-commutes with C_{2z} . For the AFM a phase (Fig. 1(d)), we find a gap of nearly 10 meV at Γ with band inversion and an indirect global bandgap of 5 meV. The double-degeneracy here is removed along $\Gamma - X$, $\Gamma - Y$, and $\Gamma - Z$, but remains along $X - S - Y$ because of antiunitary operators $\{C_{2x}|\tau\}\mathcal{T}$ and $\{M_x|\tau\}\mathcal{T}$. Details of symmetry analysis can be found in the SM Sec. III.

The presence of inversion symmetry enables us to confirm band topology by computing the parity-defined \mathbb{Z}_4 invariant [17, 18, 33],

$$\mathbb{Z}_4 = \sum_{\mathbf{k}=1}^8 \frac{n_{\mathbf{k}}^+ - n_{\mathbf{k}}^-}{2} \text{ mod } 4, \quad (2)$$

where $n_{\mathbf{k}}^{\pm}$ is the number of occupied states with \pm -parity at one of the eight inversion-invariant momenta \mathbf{k} . $\mathbb{Z}_4 = 0, 2$ indicate a trivial insulator and axion insulator, respectively, while $\mathbb{Z}_4 = 1, 3$ leads to a semimetal phase. We find that the parity change only occurs at Γ after including SOC, and \mathbb{Z}_4 invariant indicates that $\text{Eu}_3\text{In}_2\text{As}_4$ is an axion insulator in AFM phase and a topological semimetal in the FM phase, regardless of the magnetic moment orientation.

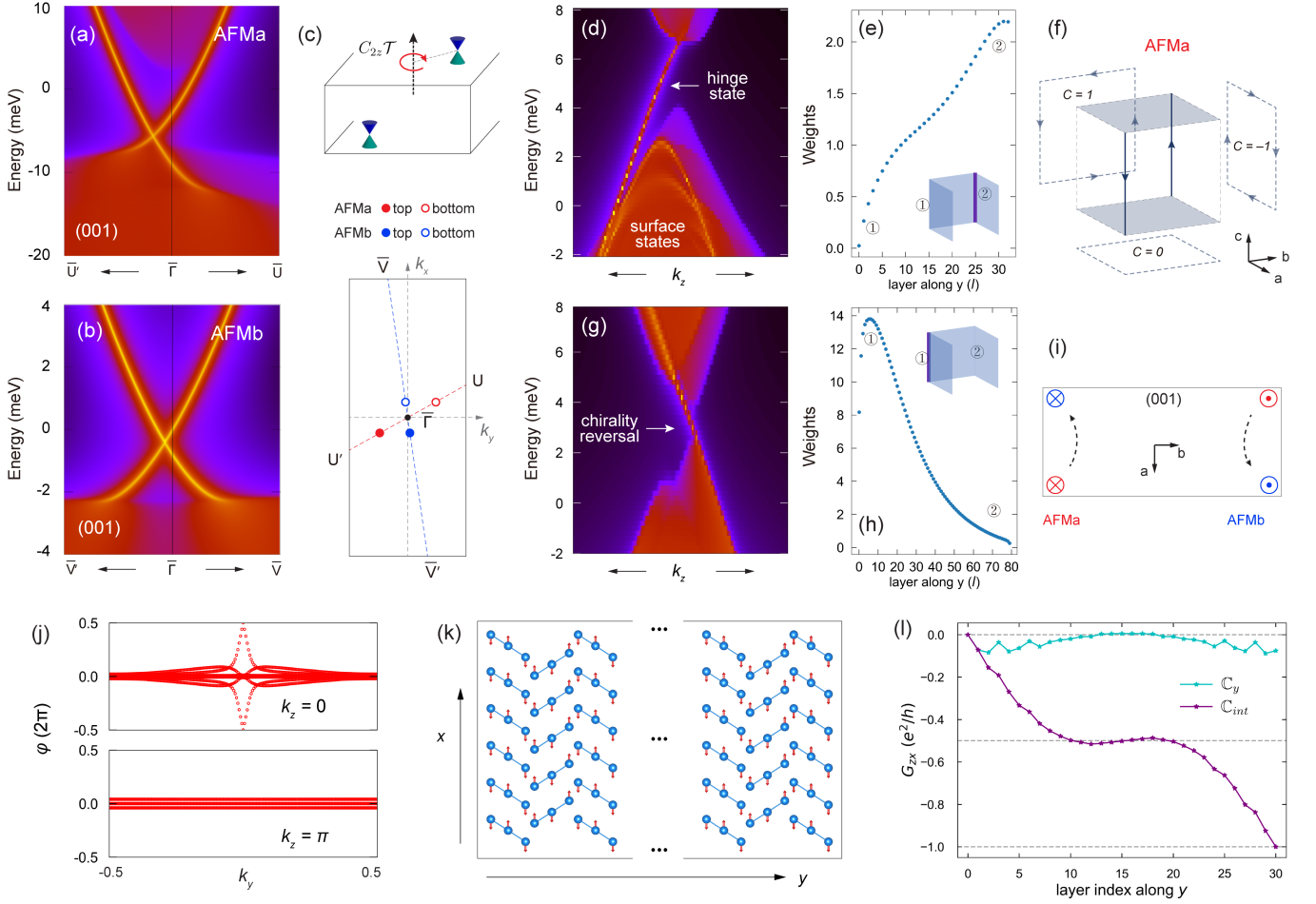


FIG. 2. Gapless surface and chiral hinge states of AFMa,b phases. (a-b) (001) Surface states. (c) Schematic illustration of the massless Dirac point under $C_{2z}\mathcal{T}$ and k -path we apply in (a-b). The BZ here is zoomed in at Γ to depict their relative positions. (d) Numerical calculations of the hinge state along c -axis, with a finite 35-unit-cell along b -axis (\hat{y}) and semi-infinite along a -axis (\hat{x}). (e) The intensity of the in-gap states projected onto each layer (unit cell), where #0 and #35 represent two hinges. The purple line denotes the real space location of the hinge states. (f) Illustration of the hinge and surface states and their Chern insulating phases projected at 2D limit along three directions. (g-h) Same as (d-e) but in AFMb phase with an 80-unit-cell along b direction. (i) Top view: chirality and position of hinge states switched between AFMa (blue) and AFMb (red) phase. (j) The 1D k_x -integrated Wilson bands as a function of k_y in $k_z = 0/\pi$ planes for the AFMa phase. (k) The inversion symmetric structure of AFMa phase implemented in hinge mode and local Chern marker calculations. (l) Local Chern number and integrated Hall conductance as a function of layer index in a 30-unit-cell slab.

III. TOPOLOGICAL SURFACE AND HINGE STATES

A. Topology of AFMa,b phases

The AFMa and AFMb phases of $\text{Eu}_3\text{In}_2\text{As}_4$ belong to the orthorhombic magnetic space group $Pnn'm'$, the generators of which include \mathcal{I} , $C_{2z}\mathcal{T}$ and $M_z\mathcal{T}$. Thus, we discuss them together in the following. In addition, the a, b, c crystallographic axes refer to $[100]$, $[010]$, and $[001]$ directions here.

The antiunitary symmetry $C_{2z}\mathcal{T}$ is helpful to understand the bulk-surface-hinge correspondence. Let us begin with a \mathcal{T} -preserved \mathbb{Z}_2 TI where all surfaces

would present Dirac surface states. For the orthorhombic crystal, magnetism opens a surface gap on bc and ac facets, *i.e.*, introduces a mass term in the Dirac equation. Because they transform to each other by $C_{2z}\mathcal{T}$, two bc facets (also two ac facets) exhibit opposite masses. For four hinges between ac and bc facets along the c direction, we can always find two diagonal hinges at the domain boundary between surfaces with opposite signs of mass, as illustrated in Fig. 2(f), leading to chiral hinge modes inside the surface gap. Although it is not respected on a single bc or ac facet, the $C_{2z}\mathcal{T}$ symmetry is preserved on the ab plane (see Fig. 2(c)) and leads to crystalline symmetry-protected unpinned Dirac surface states. In other words, the surface Dirac cone can only be pushed away from time-reversal-invariant momenta (*e.g.* Γ)

rather than gapped out by magnetism. As illustrated by Fig. 2(f), two chiral hinge states terminate at gapless ab or (001) surfaces while the equilibrium current persists, different from an ordinary higher-order TI that shows only hinge states.

Such a TCI is equivalent to a 3D strong SW insulator with vanishing Berry curvatures [10, 11, 55, 56]. Because of the antiunitary nature of $C_{2z}\mathcal{T}$, we can define a \mathbb{Z}_2 -type topological invariant $\Delta_{3D} = w_2(\pi) - w_2(0)$, where $w_2(k_z)$ is the second SW number defined on a 2D plane. The first SW number w_1 is equivalent to the quantized Berry phase and a nontrivial w_2 characterizes a double band inversion. w_2 is well-defined only when $w_1 = 0$. w_1 and w_2 can also be obtained by tracing the Wilson loop spectra φ , where w_2 is the number of crossings at $\varphi = \pi \bmod 2$. When the inversion symmetry is preserved, Δ_{3D} can be alternatively inferred from \mathbb{Z}_4 index. Fig. 2(j) indicates AFMa/ b phase as a 3D strong SW insulator with $w_2(0) = 1$ and $w_2(\pi) = 0$. The SW insulator can exhibit an odd number of Dirac cones [9, 11] on the surface with $C_{2z}\mathcal{T}$ symmetry, consistent with our analysis above.

To verify these surface and hinge states, we perform the Green's function calculations using Wannier functions extracted from DFT calculations. A single gapless Dirac cone exists on the (001) surface of AFMa/ b phases, shown in Figs. 2(a) and 2(b). Because there is no additional symmetry to constrain the Dirac point besides $C_{2z}\mathcal{T}$, the Dirac point is unpinned from $\bar{\Gamma}$ or any high-symmetry line. As depicted in Fig. 2(c), the top and bottom surface Dirac cones are transformed to each other by \mathcal{I} and thus, they are located at opposite k points. The Dirac point positions can be continuously shifted by synchronously rotating all the magnetic moments on the ab plane, for which $C_{2z}\mathcal{T}$ is maintained. In this case, the in-plane magnetic moments act as a massless perturbation for the surface Dirac cone [9].

We next investigate the hinge modes of two adjacent side facets by building a half-infinite slab model (Fig. 2(k)) [8, 33]. The obtained spectrum includes the states from bulk, one (100) surface, two (010) surfaces, and two hinges, as sketched in the inset of Fig. 2(e). Such a slab contains 34 unit cells plus half a unit cell along the b axis, which respects $C_{2z}\mathcal{T}$ and \mathcal{I} and is thick enough to suppress inter-facet and inter-hinge interactions. In Fig. 2(d), an up-moving in-gap state clearly emerges in the AFMa phase as we expect. By projecting it into each layer, we find that the spectral weight is mainly distributed at hinge ② (marked as the purple line in the inset and its wavefunction distribution on the right in Fig. 2(e)), confirming it is a hinge mode in the real space. With the assistance of the inversion symmetry, we schematically show how the gapless surface states (dark) and hinge modes distribute and flow in the real crystal in Fig. 2(f).

Thin films of such a magnetic TCI can realize the quantum anomalous Hall insulator (QAHI). By reducing this compound to the 2D in the ac/bc plane, hinge states

will be mapped to a closed-loop edge state, which enables QAHI. The corresponding Chern numbers $\mathbb{C} = \pm 1$ are opposite for the films stacking along [100] and [010] directions.

In the AFMb phase, we also discover two hinge modes with opposite chiralities. As shown in Figs. 2(g) and 2(h), a down-moving state is well localized at hinge ① (wavefunction distributes on the left). Hence, such a magnetic phase transition results in a chirality reversal and a location switch of the hinge states. Illustrated by Fig. 2(i), the hinge modes at the upper right and lower left (AFMa) will move to the lower right and upper left (AFMb), respectively, leading to the same Chern number ($\mathbb{C} = -1$) for the films stacking along [100] and [010]. Therefore, a pair of hinge states with opposite chirality could always be found in the sample with an orthorhombic geometry and their location relies on the magnetic structure, providing a way of distinguishing the Néel order between AFMa and AFMb.

The obsessing hinge states, and the gapped (100) and (010) surface states discussed above also attract us to consider what kind of transport signals or physical quantity they carry. By following [31, 57], we compute the layer-resolved local Chern marker, *i.e.*, the layer-resolved Chern number,

$$\mathbb{C}_z(l) = \frac{-4\pi}{A} \mathfrak{J} \frac{1}{N_k} \sum_{\mathbf{k}} \sum_{vv'c} X_{v\mathbf{c}\mathbf{k}} Y_{v\mathbf{c}\mathbf{k}}^\dagger \rho_{v'\mathbf{v}\mathbf{k}}(l), \quad (3)$$

where $X(Y)_{v\mathbf{c}\mathbf{k}} = \langle \psi_{v\mathbf{k}} | i\hbar v_x(y) | \psi_{c\mathbf{k}} \rangle / (E_{c\mathbf{k}} - E_{v\mathbf{k}})$ is the position operator and $\rho_{v'\mathbf{v}\mathbf{k}}(l) = \sum_{j\in l} \psi_{v'\mathbf{k}}^*(j) \psi_{v\mathbf{k}}(j)$ is the projector onto layer l , which sums over the basis j belonging to that layer. Here, we construct an AFMa-phase slab of 29 plus half unit cells along the [010] direction to apply the above formula, and the contribution of the AHC from the specific layer can be expressed as $G_{zx}(l) = \frac{e^2}{h} \mathbb{C}_y(l)$. The numerical results of $\mathbb{C}_y(l)$ and $\mathbb{C}_{int} = \sum_l \mathbb{C}_y(l)$ are shown in Fig. 2(l).

We find a saturation behavior of the half-quantized surface AHC. Such a local signal is known to be the direct evidence of the axion insulator. For the AFMa case, the thickness of more than 10 layers is enough to stabilize \mathbb{C}_{int} at 0.4976, and thus corresponds to the penetration depth of the hinge states shown in Fig. 2(e). $\mathbb{C}_y(l)$ is an even function with its origin at #15 since the sample is inversion symmetric. Distinct from AFM MnBi₂Te₄ [33], we find a single and smooth oscillation of \mathbb{C}_{int} due to the inhomogeneity of the spin moment. The internal layers from #10 to #20 tame the oscillation and they do not contribute to the total AHC. Finally, since the spin moments of the top and bottom layers hold the same direction, the half-quantized surface AHC from the first and last 10 layers together gives rise to a $\mathbb{C} = -1$ Chern insulator with in-plane magnetic moments.

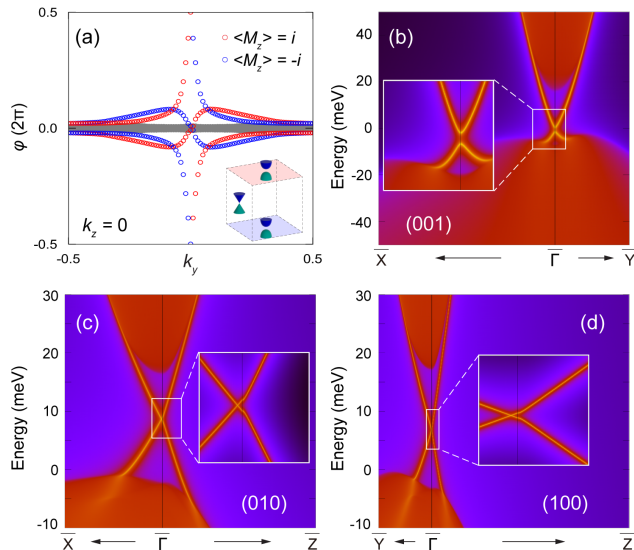


FIG. 3. Mirror-protected TCI in AFM c phase. (a) The evolution of Wannier charge center along the k_y direction for the occupied bands at mirror symmetric $k_z = 0$ plane in AFM c phase. Red and blue circles represent the mirror operation eigenvalue $\langle M_z \rangle = \pm i$. (b-d) The surface states along the high-symmetry lines of (001), (010), and (100) surfaces, respectively. The Dirac cones at $k_z = 0$ for (010) and (100) surfaces are protected by M_z symmetry.

B. Topology of AFM c phase

When the spin moments are rotated to the c direction and keep the AFM order, the magnetic space group will restore to $Pnmm$, the generators of which include \bar{I} , C_{2z} and M_z but breaks \mathcal{T} . Since a mirror symmetry always satisfies $M_z^2 = -1$ in a spinful system, its representation has eigenvalues $\pm i$. Hence, the surface states could be foreseen by calculating the mirror Chern number ($n_{M_z=\pm i}$) in two subspaces of the mirror-symmetric plane. In Fig. 3(a), our Wilson loop calculations suggest that $n_{M_z=\pm i} = \pm 1$ at $k_z = 0$ plane while $n_{M_z=\pm i} = 0$ at $k_z = \pi$ plane. Note that τ in the glide operator $\{M_{x,y}|\tau\}$ is not along a or b direction, so the surface Dirac point is not fixed at the $\bar{\Gamma}$ point, but along the $k_z = 0$ high-symmetry line at the side surfaces. In Figs. 3(b-d), the surface Green's function spectra further confirm that the magnetic moments induced a (001) surface gap (~ 2 meV) while the massless Dirac cone is fixed along $\bar{\Gamma} - \bar{X}$ of (010) and $\bar{\Gamma} - \bar{Y}$ of (100) surface. One exciting finding here is that the gapless and gapped surface states between the AFM a/b and AFM c phases are completely switched, which provides a unique playground for spintronic devices.

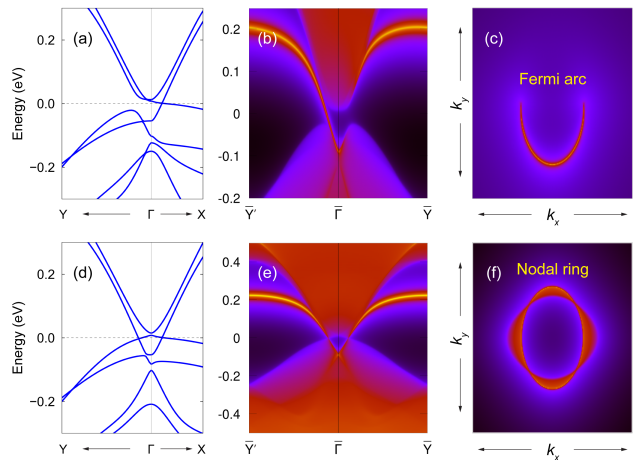


FIG. 4. Weyl semimetal in FM phase. The upper and lower panels represent the FMa and FM c phases, respectively. (a,d) Band structure near Γ point. (b,e) (100) surface energy spectrum along k_y . (c,f) Projected (001) Fermi surface, which shows that the Fermi arc connects two Weyl points and M_z protects a Weyl nodal ring.

C. Topology of FM phase

Having established the topology of the AFM phase, we next focus on the FM phases. In the FMa/ b case, we find two type-I Weyl points with opposite chiralities along $\Gamma - X/Y$ connected by \mathcal{I} in Fig. 4(a). The Wilson loop calculation, shown in Fig. S7, further confirms that $\mathbb{C} = 1$ at $k_x = 0$ plane and $\mathbb{C} = 0$ at $k_x = \pi$ plane, consistent with the band structure. We then calculate the surface state on the (100) surface (Fig. 4(b)) and project the Fermi surface onto the (001) surface (Fig. 4(c)). We find a chiral surface state connecting bulk valence and conduction bands, and the Weyl nodes separated 0.074 \AA^{-1} along k_x are connected by a surface Fermi arc. We also show in SM that the Weyl nodes in the FM b phase are shifted to locate along the $\Gamma - Y$ direction. Thus, FMa/ b phases provide an ideal Weyl semimetal, which exhibits a single pair of type-I Weyl points without extra trivial Fermi pockets at the Fermi energy. When the spin moments align along the c (FM c), corresponding magnetic space group $Pn'n'm$, the restoration of the mirror M_z will protect a nodal ring on the $k_z = 0$ plane, as shown in Fig. 4(d-f). The Berry phase integrated along a circle surrounding the nodal ring is checked to be π . Such a nodal ring leads to drumhead-like topological surface states on the (001) plane.

IV. TOPOLOGICAL PHASE DIAGRAM

This section aims to establish a unified theory for various topological phases revealed in $\text{Eu}_3\text{In}_2\text{As}_4$ by constructing a $k \cdot p$ model using the invariant theory [58], and study the global topological phase diagram for

TABLE I. The character table of $\sigma_i\tau_j\zeta_k$ matrices and the polynomials of k under time-reversal symmetry. The exchange-coupling terms $\Delta_{x,y,z}$ describe AFM*a,b,c* and $\lambda_{x,y,z}$ describe FM*a,b,c* orders, respectively.

IR	\mathcal{T}	Polynomials	$\sigma_i\tau_j\zeta_k$
Γ_1^+	+	x^2, y^2, z^2	(000)(001)(030)(031)(302)(332)
Γ_2^+	+	xy	(003)(033)
Γ_4^+	+	xz	(102)(132)
Γ_3^+	+	yz	(202)(232)
Γ_1^+	-	Δ_z	(303)(333)
Γ_2^+	-	λ_z	(002)(032)(300)(301)(330)(331)
Γ_4^+	-	Δ_x, λ_y	(103)(133)(200)(201)(230)(231)
Γ_3^+	-	Δ_y, λ_x	(100)(101)(130)(131)(203)(233)
Γ_1^-	-	xyz	(012)(023)(310)(311)
Γ_2^-	-	z, z^3, y^2z, x^2z	(020)(021)(313)(322)
Γ_4^-	-	y, yz^2, y^3, x^2y	(110)(111)(213)(222)
Γ_3^-	-	x, xz^2, xy^2, x^3	(113)(122)(210)(211)

different magnetic configurations. Because $\{C_{2y}|\tau\}$ is a key symmetry to relate two sublattices and the AFM order, three sets of Pauli matrices should be introduced to describe this system:

- spin σ : $|\frac{1}{2}\rangle$ and $|\frac{-1}{2}\rangle$

- orbital τ : $|\text{In } s\rangle$ and $|\text{As } p_z\rangle$
- sublattice ζ : $|A\rangle$ and $|B\rangle$

and the basis are labeled by $|\Lambda_\alpha, \uparrow(\downarrow)\rangle$, where $\Lambda = \text{In}, \text{As}$; $\alpha = A, B$; $\uparrow(\downarrow) = \frac{1}{2}(-\frac{1}{2})$. In the absence of magnetic order, $\text{Eu}_3\text{In}_2\text{As}_4$ is a trivial insulator. We can have the following orbital basis according to the band representation (parity \pm) and wavefunction at Γ

$$|\text{In}_A^+ s\rangle = \frac{1}{\sqrt{2}}(|\text{In}_1\rangle + |\text{In}_1'\rangle), \quad (4)$$

$$|\text{In}_B^+ s\rangle = \frac{1}{\sqrt{2}}(|\text{In}_{1*}\rangle + |\text{In}_{1*'}\rangle), \quad (5)$$

$$|\text{As}_A^- p_z\rangle = \frac{1}{\sqrt{2}}(|\text{As}_2\rangle + |\text{As}_{2'}\rangle), \quad (6)$$

$$|\text{As}_B^- p_z\rangle = \frac{1}{\sqrt{2}}(|\text{As}_{2*}\rangle + |\text{As}_{2*'}\rangle), \quad (7)$$

where the atom index $(1, 2^{*'})$ can be found in Fig. S1. The symmetry operators are thus given by $\hat{\mathcal{T}} = i\sigma_2\tau_0\zeta_0\mathcal{K}$, $\hat{\mathcal{I}} = \sigma_0\tau_3\zeta_0$, $\hat{C}_{2z} = -i\sigma_3\tau_0\zeta_0$ and $\{\hat{C}_{2y}|\tau\} = -i\sigma_2\tau_3\zeta_1$, where \mathcal{K} is the complex conjugate operator. Then we can list the irreducible representation (IR) of each matrix in Table I and Supplementary Table III. Based on that, the effective Hamiltonian is described by

$$\mathcal{H} = \mathcal{H}_{NM} + \mathcal{H}_{ex} = \begin{pmatrix} \mathcal{H}_A & \mathcal{H}_{AB} \\ \mathcal{H}_{AB}^\dagger & \mathcal{H}_B \end{pmatrix} + \begin{pmatrix} \mathcal{H}_{M,A} & \mathcal{H}_{M,AB} \\ \mathcal{H}_{M,AB}^\dagger & \mathcal{H}_{M,B} \end{pmatrix} \quad (8)$$

$$\begin{aligned} \mathcal{H}_{A/B} = & (\pm A_1 k_x + A_2 k_y)\sigma_1\tau_1 + (B_1 k_x \pm B_2 k_y)\sigma_2\tau_1 \pm C_1 k_z\sigma_3\tau_1 + D_1 k_z\sigma_0\tau_2 \\ & + (E_{01} + E_1 k_x^2 + E_2 k_y^2 + E_3 k_z^2 \pm E_4 k_x k_y)\sigma_0\tau_0 + (F_{01} + F_1 k_x^2 + F_2 k_y^2 + F_3 k_z^2 \pm F_4 k_x k_y)\sigma_0\tau_3, \end{aligned} \quad (9)$$

$$\begin{aligned} \mathcal{H}_{AB} = & A_3 k_y\sigma_1\tau_1 + B_3 k_x\sigma_2\tau_1 + D_2 k_z\sigma_0\tau_2 + (E_{02} + E_5 k_x^2 + E_6 k_y^2 + E_7 k_z^2)\sigma_0\tau_0 + (F_{02} + F_5 k_x^2 + F_6 k_y^2 + F_7 k_z^2)\sigma_0\tau_3 \\ & - i(G_0 + G_1 k_x^2 + G_2 k_y^2 + G_3 k_z^2)\sigma_3\tau_0 - iH_1 k_x k_z\sigma_1\tau_0 - iI_1 k_y k_z\sigma_2\tau_0 - iJ_1 k_x k_z\sigma_1\tau_3 - iK_1 k_y k_z\sigma_2\tau_3 \\ & - i(L_0 + L_1 k_x^2 + L_2 k_y^2 + L_3 k_z^2)\sigma_3\tau_3 - iM_1 k_x\sigma_1\tau_2 - iN_1 k_y\sigma_2\tau_2 - iO_1 k_z\sigma_3\tau_2, \end{aligned} \quad (10)$$

where F_{01} controls the bandgap [see SM Fig. S8(d)] so it can be approximately treated as the inverse of the “effective” SOC strength. Experimentally F_{01} is tuned by pnictide doping or pressure [59–61]. The bandgap closes when $F_{01} = 0.2$ eV. \mathcal{H}_A and \mathcal{H}_B are connected by $\{C_{2y}|\tau\}$ symmetry. All the other material-dependent parameters in \mathcal{H} are chosen to make dispersion close to Γ be qualitatively or semi-quantitatively consistent with the DFT bands. Since we only focus on the bands near

the Fermi level, not all the Pauli matrices above are required to be activated.

We next consider the exchange coupling terms \mathcal{H}_{ex} , namely \mathcal{T} -odd terms when introducing magnetic orders. Note that the AFM*a* phase shares the same IR with FM*b* (also for AFM*b* and FM*a*), so both the on-site terms $\sigma_1\tau_0\zeta_3$ and $\sigma_2\tau_0\zeta_0$ will couple with IR Γ_4^+ . Generally, $\mathbf{m} \cdot \boldsymbol{\sigma}$ could be taken to characterize the magnetization of one sublattice and thus to distinguish them [17]. Take

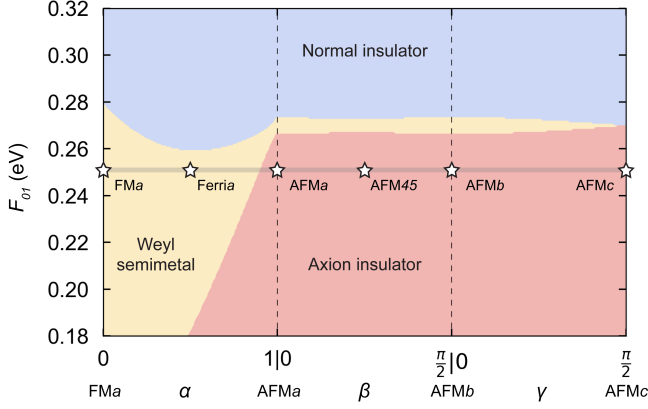


FIG. 5. Topological phase diagram in terms of SOC strength F_{01} and magnetic orders α, β, γ (see text). Pentagrams along the gray line represent DFT results for $\text{Eu}_3\text{In}_2\text{As}_4$.

the AFMa phase as an example, we have

$$\mathcal{H}_{\text{AFMa}, A/B} = \pm \Delta_{x1} \sigma_1 \tau_0 \pm \Delta_{x2} \sigma_1 \tau_3, \quad (11)$$

$$\mathcal{H}_{\text{AFMb}, A/B} = \lambda_{y1} \sigma_2 \tau_0 + \lambda_{y2} \sigma_2 \tau_3, \quad (12)$$

$$\mathcal{H}_{\text{AFMa}/\text{AFMb}, AB} = \Delta_3 \sigma_2 \tau_0 + \Delta_4 \sigma_2 \tau_3. \quad (13)$$

Similarly, the exchange terms for the FMa, AFMb, and AFMc phases can be obtained, respectively. Additionally, the intermediate phases between them, namely $C_{2z}\mathcal{T}$ -preserved ferrimagnetic and tilted AFM orders, can be expressed as the linear combination

$$\mathcal{H}_{\text{Ferria}} = \alpha \cdot \mathcal{H}_{\text{AFMa}} + (1 - \alpha) \cdot \mathcal{H}_{\text{FMa}}, \quad (14)$$

$$\mathcal{H}_{\text{AFM}'} = \cos \beta \cdot \mathcal{H}_{\text{AFMa}} + \sin \beta \cdot \mathcal{H}_{\text{AFMb}}, \quad (15)$$

$$\mathcal{H}_{\text{AFM}''} = \cos \gamma \cdot \mathcal{H}_{\text{AFMb}} + \sin \gamma \cdot \mathcal{H}_{\text{AFMc}}. \quad (16)$$

By numerically solving the model, we construct a \mathcal{T} -broken phase diagram (Fig. 5) as functions of F_{01} and α, β, γ . We find $\text{Eu}_3\text{In}_2\text{As}_4$ can be very well mapped onto the grey horizontal line with $F_{01} = 0.25$ eV. Thanks to the large exchange field of Eu^{2+} cations, the phase transition boundary is advanced to lie around 0.27 eV, accompanied by a gap closing and reopening. As an intermediate region between two insulating phases [62], the chance of being a Weyl semimetal is intimately related to the magnetic configuration. Within the FM order, the Zeeman effect results in a large semimetallic region. Then it shrinks to a fairly narrow range in the AFMa/b or tilted phase, and eventually vanishes in the AFMc phase for the double degeneracy of the bands. We can see the axion angle $\theta = \pi$ is quite robust against the perturbation on orientations of the AFM order in $\text{Eu}_3\text{In}_2\text{As}_4$. The model parameters and DFT verification (marked white stars) are provided in SM Sec. VI.

V. DISCUSSIONS AND CONCLUSIONS

Our results so far demonstrate that this highly tunable platform $\text{Eu}_3\text{In}_2\text{As}_4$ enables a variety of topological phases. One may next wonder what the universal feature of the bulk-surface-hinge correspondence for the whole $\text{Eu}_{2n+1}\text{In}_2\text{As}(\text{Sb})_{2n+2}$ family ($n = 0, 1, 2, \dots$). We first notice that EuIn_2As_2 is quite special as a hexagonal lattice but $\text{Eu}_3\text{In}_2\text{As}_4$ and $\text{Eu}_5\text{In}_2\text{As}_6$ are orthorhombic [18, 54, 59–61]. Since surface and hinge states are closely associated with geometries, their commonalities must be analyzed under a unified crystalline representation. More importantly, $C_2\mathcal{T}$ is preserved in their DFT calculated magnetic ground states but absent on the surfaces of hexagonal prisms. With a lattice transformation of EuIn_2As_2 , we found nontrivial w_2 number by the Wilson-loop and $C_2\mathcal{T}$ protected Dirac surface states in SM Sec. IV. The Dirac point is constrained at the $\bar{\Gamma}-\bar{Z}$ line rather than completely unpinned due to the $\{M_y|(0, 0, c/2)\}$ symmetry.

$\text{Eu}_3\text{In}_2\text{As}_4$ nanowires were recently grown from InAs nanowires by a topotaxial mutual-exchange method [52] and can inherit good interface quality to the ordinary superconductor (*e.g.*, Al) [53]. Because of the intrinsic magnetism, strong SOC effect, and topological surface states, $\text{Eu}_3\text{In}_2\text{As}_4$ paves an appealing avenue to explore Majorana physics, as illustrated in Fig. 6. The intrinsic magnetism and SOC together lift the spin degeneracy and an odd number of Fermi surfaces can be realized at an accessible chemical potential, which

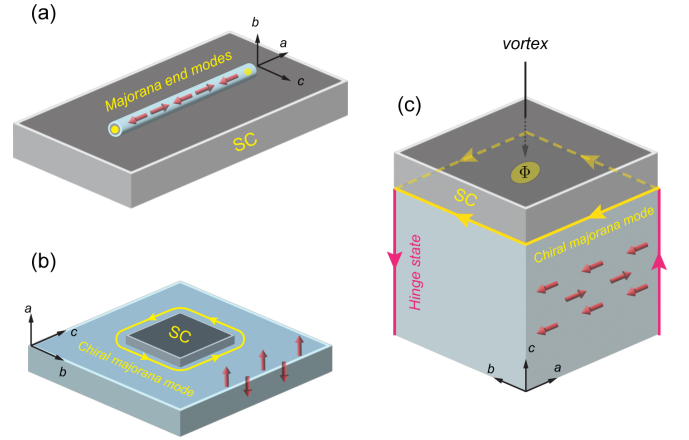


FIG. 6. Schematics of the axion insulator $\text{Eu}_3\text{In}_2\text{As}_4$ (cyan-blue) in proximity to an s -wave superconductor (SC) (grey). (a) The nanowire configuration. (b) The SC proximity to the gapped surface, *e.g.*, the ac/bc surfaces in AFMa phase. (c) The SC proximity to the gapless surface, *e.g.*, the ab surface in AFMa phase. One chiral hinge state (pink lines) splits into two chiral Majorana edge modes, providing an interferometer configuration. The white circle indicates a vortex inside the interferometer. Yellow lines (dots) represent the chiral Majorana modes (Majorana end modes). The red arrows represent spin moments in the axion insulator.

is the precondition to design structure with Majorana [63]. (i) In a nanowire configuration [64, 65], the finite size effect gaps the hinge and surface states, leading to nondegenerate topology-driven nanowire bands. In proximity to an *s*-wave superconductor, localized zero-energy Majorana modes will arise at two ends. Compared to earlier proposals [66, 67], we do not require an external magnetic field to break time-reversal symmetry here. (ii) On the gapped surface (e.g., *ac/bc* facet in AFMa), one can deposit a superconductor island and expect chiral Majorana edge states around the island, if the superconductor's gap Δ overcomes the magnetization-induced surface gap $h \sim 2$ meV. Using Fu and Kane's proposal [3, 63], we expect a stable nontrivial pairing by covering a superconductor on *ac* or *bc* surfaces (criterion $|h| < \Delta$ when Fermi energy lies inside the gap). In this case, 1D chiral Majorana modes appear at the interface between the axion insulator's surface and a superconductor region [68]. If the Fermi energy crosses an odd number of Dirac bands (metallic regime), similar chiral Majorana modes also appear in this case. (iii) On the gapless surface (e.g., *ab* facet in AFMa), covering a superconductor on the whole surface may lead to co-propagating 1D chiral Majorana edge modes. Two Majorana modes merge into one chiral electronic state at the hinge [69]. As illustrated by Fig. 6c, two chiral Majorana modes and two chiral hinge states naturally form a Mach-Zehnder interferometer, in which

the conductance between two chiral hinge modes depends on the parity of the number of enclosed vortices in the superconductor region [68, 70].

In summary, we propose that $\text{Eu}_3\text{In}_2\text{As}_4$ is an AFM axion insulator and exhibits hybrid-order topological states. By establishing a $C_2\mathcal{T}$ governed framework, the unpinned Dirac surface, chiral hinge states, and half-quantized surface AHC are unveiled. Since the single crystal and nanowire of $\text{Eu}_3\text{In}_2\text{As}_4$ are readily synthesized, angle-resolved photoemission spectroscopy (ARPES), scanning tunneling spectroscopy (STS) and other techniques are called to detect these topological surface states, hinge states, and Weyl points/Fermi arcs and explore their coupling to magnetism and superconductivity.

ACKNOWLEDGMENTS

We are inspired by a recent experiment work by Haim Beidenkopf and Hadas Shtrikman. We thank helpful discussions with Xi Dai, Mingqiang Gu and Hengxin Tan. B.Y. acknowledges the financial support by the European Research Council (ERC Consolidator Grant "NonlinearTopo", No. 815869) and the ISF - Personal Research Grant (No. 2932/21). C.-X. L. also acknowledges the support of NSF Grant No. (DMR-2241327)

-
- [1] M. Z. Hasan and C. L. Kane, Colloquium: Topological insulators, *Rev. Mod. Phys.* **82**, 3045 (2010).
- [2] X.-L. Qi and S.-C. Zhang, Topological insulators and superconductors, *Reviews of Modern Physics* **83**, 1057 (2011).
- [3] Y. Tokura, K. Yasuda, and A. Tsukazaki, Magnetic topological insulators, *Nature Reviews Physics* **1**, 126 (2019).
- [4] Y. Chen, J. G. Analytis, J.-H. Chu, Z. Liu, S.-K. Mo, X.-L. Qi, H. Zhang, D. Lu, X. Dai, Z. Fang, *et al.*, Experimental realization of a three-dimensional topological insulator, *science* **325**, 178 (2009).
- [5] H. Zhang, C.-X. Liu, X.-L. Qi, X. Dai, Z. Fang, and S.-C. Zhang, Topological insulators in Bi_2Se_3 , Bi_2Te_3 and Sb_2Te_3 with a single dirac cone on the surface, *Nature physics* **5**, 438 (2009).
- [6] T. H. Hsieh, H. Lin, J. Liu, W. Duan, A. Bansil, and L. Fu, Topological crystalline insulators in the snr material class, *Nature communications* **3**, 982 (2012).
- [7] F. Schindler, Z. Wang, M. G. Vergniory, A. M. Cook, A. Murani, S. Sengupta, A. Y. Kasumov, R. Deblock, S. Jeon, I. Drozdov, *et al.*, Higher-order topology in bismuth, *Nature physics* **14**, 918 (2018).
- [8] C. Yue, Y. Xu, Z. Song, H. Weng, Y.-M. Lu, C. Fang, and X. Dai, Symmetry-enforced chiral hinge states and surface quantum anomalous hall effect in the magnetic axion insulator $\text{Bi}_{2-x}\text{Sm}_x\text{Se}_3$, *Nature Physics* **15**, 577 (2019).
- [9] C. Fang and L. Fu, New classes of three-dimensional topological crystalline insulators: Nonsymmorphic and magnetic, *Phys. Rev. B* **91**, 161105 (2015).
- [10] J. Ahn, D. Kim, Y. Kim, and B.-J. Yang, Band topology and linking structure of nodal line semimetals with Z_2 monopole charges, *Phys. Rev. Lett.* **121**, 106403 (2018).
- [11] J. Ahn and B.-J. Yang, Symmetry representation approach to topological invariants in $C_{2z}t$ -symmetric systems, *Phys. Rev. B* **99**, 235125 (2019).
- [12] R. González-Hernández, C. Pinilla, and B. Uribe, Axion insulators protected by $C_2\mathcal{T}$ symmetry, their *k*-theory invariants, and material realizations, *Phys. Rev. B* **106**, 195144 (2022).
- [13] W. A. Benalcazar, B. A. Bernevig, and T. L. Hughes, Quantized electric multipole insulators, *Science* **357**, 61 (2017).
- [14] Z. Song, Z. Fang, and C. Fang, (d-2)-dimensional edge states of rotation symmetry protected topological states, *Physical review letters* **119**, 246402 (2017).
- [15] Z. Wang, B. J. Wieder, J. Li, B. Yan, and B. A. Bernevig, Higher-order topology, monopole nodal lines, and the origin of large fermi arcs in transition metal dichalcogenides xTe_2 ($x = \text{Mo}, \text{W}$), *Phys. Rev. Lett.* **123**, 186401 (2019).
- [16] J. Langbehn, Y. Peng, L. Trifunovic, F. von Oppen, and P. W. Brouwer, Reflection-symmetric second-order topological insulators and superconductors, *Physical review letters* **119**, 246401 (2017).
- [17] R.-X. Zhang, F. Wu, and S. D. Sarma, Möbius insulator and higher-order topology in $\text{mmbi}_{2n}\text{te}_{3n+1}$, *Physical*

- review letters **124**, 136407 (2020).
- [18] Y. Xu, Z. Song, Z. Wang, H. Weng, and X. Dai, Higher-order topology of the axion insulator euin_2as_2 , *Phys. Rev. Lett.* **122**, 256402 (2019).
- [19] K. Yasuda, M. Mogi, R. Yoshimi, A. Tsukazaki, K. S. Takahashi, M. Kawasaki, F. Kagawa, and Y. Tokura, Quantized chiral edge conduction on domain walls of a magnetic topological insulator, *Science* **358**, 1311 (2017).
- [20] R. S. K. Mong, A. M. Essin, and J. E. Moore, Antiferromagnetic topological insulators, *Phys. Rev. B* **81**, 245209 (2010).
- [21] D. Zhang, M. Shi, T. Zhu, D. Xing, H. Zhang, and J. Wang, Topological axion states in the magnetic insulator mnbi_2te_4 with the quantized magnetoelectric effect, *Phys. Rev. Lett.* **122**, 206401 (2019).
- [22] J. Li, Y. Li, S. Du, Z. Wang, B.-L. Gu, S.-C. Zhang, K. He, W. Duan, and Y. Xu, Intrinsic magnetic topological insulators in van der waals layered mnbi_2te_4 -family materials, *Science Advances* **5**, eaaw5685 (2019).
- [23] M. M. Otrokov, I. P. Rusinov, M. Blanco-Rey, M. Hoffmann, A. Y. Vyazovskaya, S. V. Eremeev, A. Ernst, P. M. Echenique, A. Arnau, and E. V. Chulkov, Unique thickness-dependent properties of the van der waals interlayer antiferromagnet mnbi_2te_4 films, *Phys. Rev. Lett.* **122**, 107202 (2019).
- [24] X.-L. Qi, T. L. Hughes, and S.-C. Zhang, Topological field theory of time-reversal invariant insulators, *Phys. Rev. B* **78**, 195424 (2008).
- [25] F. Wilczek, Two applications of axion electrodynamics, *Phys. Rev. Lett.* **58**, 1799 (1987).
- [26] A. M. Essin, J. E. Moore, and D. Vanderbilt, Magnetoelectric polarizability and axion electrodynamics in crystalline insulators, *Phys. Rev. Lett.* **102**, 146805 (2009).
- [27] N. P. Armitage and L. Wu, On the matter of topological insulators as magnetoelectrics, *SciPost Physics* **6**, 046 (2019).
- [28] C. Fang, M. J. Gilbert, and B. A. Bernevig, Bulk topological invariants in noninteracting point group symmetric insulators, *Physical Review B* **86**, 115112 (2012).
- [29] A. Sekine and K. Nomura, Axion electrodynamics in topological materials, *Journal of Applied Physics* **129**, 141101 (2021).
- [30] C.-Z. Chang, C.-X. Liu, and A. H. MacDonald, Colloquium: Quantum anomalous hall effect, *Rev. Mod. Phys.* **95**, 011002 (2023).
- [31] N. Varnava and D. Vanderbilt, Surfaces of axion insulators, *Phys. Rev. B* **98**, 245117 (2018).
- [32] O. Pozo, C. Repellin, and A. G. Grushin, Quantization in chiral higher order topological insulators: Circular dichroism and local chern marker, *Phys. Rev. Lett.* **123**, 247401 (2019).
- [33] M. Gu, J. Li, H. Sun, Y. Zhao, C. Liu, J. Liu, H. Lu, and Q. Liu, Spectral signatures of the surface anomalous hall effect in magnetic axion insulators, *Nature communications* **12**, 3524 (2021).
- [34] C.-Z. Chang, J. Zhang, X. Feng, J. Shen, Z. Zhang, M. Guo, K. Li, Y. Ou, P. Wei, L.-L. Wang, *et al.*, Experimental observation of the quantum anomalous hall effect in a magnetic topological insulator, *Science* **340**, 167 (2013).
- [35] M. Mogi, M. Kawamura, R. Yoshimi, A. Tsukazaki, Y. Kozuka, N. Shirakawa, K. Takahashi, M. Kawasaki, and Y. Tokura, A magnetic heterostructure of topological insulators as a candidate for an axion insulator, *Nature materials* **16**, 516 (2017).
- [36] M. Mogi, M. Kawamura, A. Tsukazaki, R. Yoshimi, K. S. Takahashi, M. Kawasaki, and Y. Tokura, Tailoring tricolor structure of magnetic topological insulator for robust axion insulator, *Science advances* **3**, eaao1669 (2017).
- [37] C.-Z. Chang, W. Zhao, D. Y. Kim, H. Zhang, B. A. Assaf, D. Heiman, S.-C. Zhang, C. Liu, M. H. Chan, and J. S. Moodera, High-precision realization of robust quantum anomalous hall state in a hard ferromagnetic topological insulator, *Nature materials* **14**, 473 (2015).
- [38] Y. Feng, X. Feng, Y. Ou, J. Wang, C. Liu, L. Zhang, D. Zhao, G. Jiang, S.-C. Zhang, K. He, *et al.*, Observation of the zero hall plateau in a quantum anomalous hall insulator, *Physical review letters* **115**, 126801 (2015).
- [39] X. Kou, L. Pan, J. Wang, Y. Fan, E. S. Choi, W.-L. Lee, T. Nie, K. Murata, Q. Shao, S.-C. Zhang, *et al.*, Metal-to-insulator switching in quantum anomalous hall states, *Nature communications* **6**, 8474 (2015).
- [40] M. M. Otrokov, I. I. Klimovskikh, H. Bentmann, D. Estyunin, A. Zeugner, Z. S. Aliev, S. Gaß, A. Wolter, A. Koroleva, A. M. Shikin, *et al.*, Prediction and observation of an antiferromagnetic topological insulator, *Nature* **576**, 416 (2019).
- [41] Y. Deng, Y. Yu, M. Z. Shi, Z. Guo, Z. Xu, J. Wang, X. H. Chen, and Y. Zhang, Quantum anomalous hall effect in intrinsic magnetic topological insulator mnbi_2te_4 , *Science* **367**, 895 (2020).
- [42] C. Liu, Y. Wang, H. Li, Y. Wu, Y. Li, J. Li, K. He, Y. Xu, J. Zhang, and Y. Wang, Robust axion insulator and chern insulator phases in a two-dimensional antiferromagnetic topological insulator, *Nature materials* **19**, 522 (2020).
- [43] H. Li, S.-Y. Gao, S.-F. Duan, Y.-F. Xu, K.-J. Zhu, S.-J. Tian, J.-C. Gao, W.-H. Fan, Z.-C. Rao, J.-R. Huang, J.-J. Li, D.-Y. Yan, Z.-T. Liu, W.-L. Liu, Y.-B. Huang, Y.-L. Li, Y. Liu, G.-B. Zhang, P. Zhang, T. Kondo, S. Shin, H.-C. Lei, Y.-G. Shi, W.-T. Zhang, H.-M. Weng, T. Qian, and H. Ding, Dirac surface states in intrinsic magnetic topological insulators eusn_2as_2 and $\text{mnbi}_{2n}\text{te}_{3n+1}$, *Phys. Rev. X* **9**, 041039 (2019).
- [44] T. Sato, Z. Wang, D. Takane, S. Souma, C. Cui, Y. Li, K. Nakayama, T. Kawakami, Y. Kubota, C. Cacho, T. K. Kim, A. Arab, V. N. Strocov, Y. Yao, and T. Takahashi, Signature of band inversion in the antiferromagnetic phase of axion insulator candidate euin_2as_2 , *Phys. Rev. Res.* **2**, 033342 (2020).
- [45] X. Gui, I. Pletikoscic, H. Cao, H.-J. Tien, X. Xu, R. Zhong, G. Wang, T.-R. Chang, S. Jia, T. Valla, *et al.*, A new magnetic topological quantum material candidate by design, *ACS central science* **5**, 900 (2019).
- [46] G. M. Pierantozzi, A. De Vita, C. Bigi, X. Gui, H.-J. Tien, D. Mondal, F. Mazzola, J. Fujii, I. Vobornik, G. Vinai, *et al.*, Evidence of magnetism-induced topological protection in the axion insulator candidate eusn_2p_2 , *Proceedings of the National Academy of Sciences* **119**, e2116575119 (2022).
- [47] S. X. Riberolles, T. V. Trevisan, B. Kuthanazhi, T. Heitmann, F. Ye, D. Johnston, S. Bud'ko, D. Ryan, P. Canfield, A. Kreyssig, *et al.*, Magnetic crystalline-symmetry-protected axion electrodynamics and field-tunable unpinned dirac cones in euin_2as_2 , *Nature*

- communications **12**, 999 (2021).
- [48] L. Šmejkal, J. Sinova, and T. Jungwirth, Beyond conventional ferromagnetism and antiferromagnetism: A phase with nonrelativistic spin and crystal rotation symmetry, *Phys. Rev. X* **12**, 031042 (2022).
- [49] L. Šmejkal, J. Sinova, and T. Jungwirth, Emerging research landscape of altermagnetism, *Phys. Rev. X* **12**, 040501 (2022).
- [50] J. Krempaský, L. Šmejkal, S. D'Souza, M. Hajlaoui, G. Springholz, K. Uhlířová, F. Alarab, P. Constantinou, V. Strocov, D. Usanov, *et al.*, Altermagnetic lifting of kramers spin degeneracy, *Nature* **626**, 517 (2024).
- [51] Y.-P. Zhu, X. Chen, X.-R. Liu, Y. Liu, P. Liu, H. Zha, G. Qu, C. Hong, J. Li, Z. Jiang, *et al.*, Observation of plaid-like spin splitting in a noncoplanar antiferromagnet, *Nature* **626**, 523 (2024).
- [52] M. S. Song *et al.*, Topotaxial mutual-exchange growth of magnetic zintl eu₃in₂as₄ nanowires with axion insulator classification, under review (2024).
- [53] A. Das, Y. Ronen, Y. Most, Y. Oreg, M. Heiblum, and H. Shtrikman, Zero-bias peaks and splitting in an alinas nanowire topological superconductor as a signature of majorana fermions, *Nature Physics* **8**, 887 (2012).
- [54] A. B. Childs, S. Baranets, and S. Bobev, Five new ternary indium-arsenides discovered. synthesis and structural characterization of the zintl phases sr₃in₂as₄, ba₃in₂as₄, eu₃in₂as₄, sr₅in₂as₆ and eu₅in₂as₆, *Journal of Solid State Chemistry* **278**, 120889 (2019).
- [55] M. Pan, D. Li, J. Fan, and H. Huang, Two-dimensional stiefel-whitney insulators in liganded xenes, *npj Computational Materials* **8**, 1 (2022).
- [56] Z. Guo, J. Deng, Y. Xie, and Z. Wang, Quadrupole topological insulators in ta₂m₃te₅ (m= ni, pd) monolayers, *npj Quantum Materials* **7**, 87 (2022).
- [57] A. Marrazzo and R. Resta, Locality of the anomalous hall conductivity, *Phys. Rev. B* **95**, 121114 (2017).
- [58] C.-X. Liu, X.-L. Qi, H. Zhang, X. Dai, Z. Fang, and S.-C. Zhang, Model hamiltonian for topological insulators, *Phys. Rev. B* **82**, 045122 (2010).
- [59] N. Varnava, T. Berry, T. M. McQueen, and D. Vanderbilt, Engineering magnetic topological insulators in eu 5 m 2 x 6 zintl compounds, *Physical Review B* **105**, 235128 (2022).
- [60] M. V. A. Crivillero, S. Rößler, P. F. Rosa, J. Müller, U. Rößler, and S. Wirth, Surface and electronic structure at atomic length scales of the nonsymmorphic antiferromagnet eu₅in₂sb₆, *Physical Review B* **106**, 035124 (2022).
- [61] P. Rosa, Y. Xu, M. Rahn, J. Souza, S. Kushwaha, L. Veiga, A. Bombardi, S. Thomas, M. Janoschek, E. Bauer, *et al.*, Colossal magnetoresistance in a non-symmorphic antiferromagnetic insulator, *npj Quantum Materials* **5**, 52 (2020).
- [62] A. A. Burkov and L. Balents, Weyl semimetal in a topological insulator multilayer, *Phys. Rev. Lett.* **107**, 127205 (2011).
- [63] L. Fu and C. L. Kane, Superconducting proximity effect and majorana fermions at the surface of a topological insulator, *Phys. Rev. Lett.* **100**, 096407 (2008).
- [64] R. M. Lutchyn, J. D. Sau, and S. Das Sarma, Majorana fermions and a topological phase transition in semiconductor-superconductor heterostructures, *Phys. Rev. Lett.* **105**, 077001 (2010).
- [65] Y. Oreg, G. Refael, and F. von Oppen, Helical liquids and majorana bound states in quantum wires, *Phys. Rev. Lett.* **105**, 177002 (2010).
- [66] A. Cook and M. Franz, Majorana fermions in a topological-insulator nanowire proximity-coupled to an s-wave superconductor, *Phys. Rev. B* **84**, 201105 (2011).
- [67] J. Alicea, New directions in the pursuit of majorana fermions in solid state systems, *Reports on progress in physics* **75**, 076501 (2012).
- [68] A. R. Akhmerov, J. Nilsson, and C. W. J. Beenakker, Electrically detected interferometry of majorana fermions in a topological insulator, *Phys. Rev. Lett.* **102**, 216404 (2009).
- [69] J. Wang, Q. Zhou, B. Lian, and S.-C. Zhang, Chiral topological superconductor and half-integer conductance plateau from quantum anomalous hall plateau transition, *Phys. Rev. B* **92**, 064520 (2015).
- [70] L. Fu and C. L. Kane, Probing neutral majorana fermion edge modes with charge transport, *Phys. Rev. Lett.* **102**, 216403 (2009).